Magnetic Resonance Materials in Physics, Biology and Medicine
https://doi.org/10.1007/s10334-026-01420-0

RESEARCH ARTICLE

Design of a nonlinear double-breast single-axis gradient coil with controlled anterior–posterior gradient variation for diffusion-weighted imaging

Feng Jia[1] · **Gerrit C. Arends**[2] · **Philipp Amrein**[1,4] · **Edwin Versteeg**[2] · **Dennis W. J. Klomp**[2] · **Maxim Zaitsev**[1] · **Chantal M. W. Tax**[2,3] · **Sebastian Littin**[1]

Received: 2 April 2026 / Revised: 20 August 2026 / Accepted: 24 August 2026

Abstract

Introduction High-performance whole-body gradient systems show promise for breast diffusion-weighted imaging, but their performance is constrained by physiological limits. Although local nonlinear gradient coils can provide stronger gradients while remaining within these limits, they often exhibit a substantial reduction in the gradient amplitude of the z-component of the magnetic field near the chest wall.

Methods We introduced an optimization framework incorporating a constraint on the anterior–posterior variation in the encoding gradient amplitude. A figure of merit combining coil efficiency and minimum wire width was defined to assess performance. A prototype was constructed to validate the design methodology.

Results The optimized coil achieved a 2.35-fold efficiency increase over standard linear coils. Compared to previous nonlinear designs, the new constraint reduced spatial variation by 35.7% and improved minimum efficiency near the chest wall by 2.6-fold. Experimental field maps matched simulations with errors under 8%.

Discussion The proposed method effectively mitigates the trade-off between gradient strength and spatial uniformity along anterior–posterior direction. By enhancing performance in the posterior breast region, the design addresses a critical limitation of previous local coils.

Conclusion This framework enables the development of high-performance, robust local gradient coils, facilitating the clinical implementation of advanced DWI protocols for breast cancer screening.

Keywords Magnetic resonance imaging · Gradient coil design · Diffusion weighted imaging · Non-linear spatial encoding magnetic fields

Introduction

Breast cancer is the most common malignancy in women globally and a leading cause of cancer-related mortality, highlighting the necessity for effective screening and early detection strategies. Magnetic resonance imaging (MRI) has become an indispensable modality in breast cancer diagnostics, particularly for high-risk populations and women with dense breast tissue, where mammography sensitivity is limited [1]. Screening-compatible MR protocols must be short, robust, and quantitative. In a clinical MRI scanner, two pulse-sequence pillars are dynamic contrast-enhanced (DCE) MRI and diffusion-weighted imaging (DWI). Preliminary evidence suggests that DWI could be an alternative to DCE MRI for breast cancer screening while avoiding gadolinium risks [2, 3].

✉ Feng Jia
feng.jia@uniklinik-freiburg.de

1 Division of Medical Physics, Department of Diagnostic and Interventional Radiology, Medical Center-University of Freiburg, Faculty of Medicine, University of Freiburg, Freiburg, Germany

2 Center for Image Sciences, University Medical Center Utrecht, Utrecht, The Netherlands

3 School of Physics and Astronomy, Cardiff University Brain Research Imaging Centre (CUBRIC), Cardiff University, Cardiff, UK

4 Department of Radiology, Athinoula A Martinos Center for Biomedical Imaging, Massachusetts General Hospital, Charlestown, MA, USA

Published online: 19 September 2026

For DWI, high b-value diffusion encoding and short echo time (TE) are important to improve lesion conspicuity [4] and quantitative biomarkers such as the apparent diffusion coefficient (ADC) [5]. However, shorter TE for the same b-value is strongly constrained by gradient performance: the maximum gradient strength and slew rate [6–10]. At present the highest-performance whole-body gradient system with 300 mT/m gradient strength is a part of the experimental Connectome whole-body sized scanner [7]. However, the main limitation of such gradient systems is posed by physiology, namely the need to avoid peripheral nerve stimulation (PNS) and cardiac stimulation [7]. PNS limitations inversely correlate to the size of the gradient coil. Therefore smaller and more localized gradients allow circumventing PNS limitations [11, 12].

Nonlinear gradient coils allow for generating even higher gradient amplitudes locally than conventional linear local gradient coils. We have recently introduced a nonlinear local single-breast gradient coil optimized to maximize the gradient amplitude regardless of its orientation. This coil is capable of producing a gradient strength of over 1 T/m [13, 14] for diffusion-weighted imaging, in which spatial information is encoded through the spatial variation of the z-component of the magnetic field, assuming that the main magnetic field is oriented along the z-axis. However, a large variation of the encoding gradient amplitudes along the anterior–posterior (y-axis) direction limits the diagnostic value of this setup close to the chest wall. To address this, our current work introduces a novel constraint in the coil design to control y-axis gradient variation.

In addition to the need for higher gradient amplitudes, several engineering constraints, such as sufficiently wide wire tracks, need be considered in the design of a local breast coil. Typically, the minimum width of the coil wire tracks limits the maximum current that can flow through the wire, thereby restricting the achievable maximum encoding gradient for imaging. In this study, we propose a novel figure of merit (FOM) that relates to both minimum wire width and gradient coil efficiency. This figure of merit is used to evaluate coil performance and guide the formulation of design optimization problems. Using this optimization framework, a double-breast nonlinear gradient coil was designed for cancer screening, and a prototype was constructed to demonstrate the validity of the design methodology.

Methods

A wire-width-based performance measure

To establish a figure of merit related to the minimum wire width for a nonlinear coil, it is important to first examine the corresponding performance parameter used to evaluate a conventional linear coil. In the context of a linear gradient coil, the wire-width-based figure of merit β_J is defined as $\beta_J := \eta w_{\min}$, as outlined in [15]. Here, $w_{\min}$ represents the minimum wire width, and η signifies the efficiency of the linear gradient coil. The coil efficiency η (T/(m·A)) is defined as the ratio of the gradient amplitude G of the magnetic encoding field generated by the coil to the coil current I, expressed as $\eta := G/I$ [16]. β_J has the units of T/A when $w_{\min}$ is given in meters. Typically, the value of G is calculated at the origin [16] or at the center of a region of interest (ROI) [17] for a linear coil. Therefore, we can deduce that $\beta_J = Gw_{\min}/I = G/|\vec{J}|_{\max}$, where $|\vec{J}|_{\max}$ indicates the maximum norm of the electrical current density vector $\vec{J}$ flowing through a current-carrying surface.

For nonlinear coils, the gradient strength of encoding fields typically exhibits spatial variation within the ROI. To capture a meaningful nonlinear encoding field within the ROI, it is logical to aggregate the gradient strength over all test points in the ROI. This aggregate is then considered in the definition of a wire-width-based figure of merit for a nonlinear coil. Based on these considerations, the wire-width-based FOM is defined as follows:

$$\beta_J := \frac{\sum_{\vec{x}_i \in \mathrm{ROI}} |\nabla B_z(\vec{x}_i)|}{kI} w_{\min} = \frac{\sum_{\vec{x}_i \in \mathrm{ROI}} |\nabla B_z(\vec{x}_i)|}{k|\vec{J}|_{\max}} = \bar{\eta} w_{\min}. \tag{1}$$

Here, k denotes the total number of test points $\vec{x}_i$ in the ROI, and $\bar{\eta}$ is the average coil efficiency, given by $\bar{\eta} := \sum_{\vec{x}_i \in \mathrm{ROI}} |\nabla B_z(\vec{x}_i)|/(kI)$. The B_z is the z-component of the magnetic field $\vec{B}$ generated by current density $\vec{J}$, which is calculated using the Biot–Savart law. Note that the formula (1) for β_J can also be utilized for calculations of the wire-width-based FOM for a linear coil in subsequent examples, enabling fair comparisons between the performance of linear and nonlinear coils.

According to Eq. (1), a larger β_J for a coil implies a higher average coil efficiency over the ROI for a given minimum wire width of the coil. That also means that the coil generates higher average gradient strength when a fixed current was applied to the coil with a given minimum wire width.

Formulation of the optimization problem

To propose a suitable optimization problem in the design of a nonlinear breast coil for diffusion weighting, several requirements were considered. The first requirement was that the coil generated an encoding field with strong gradients within the ROI. Given that the minimum wire width of a coil was based on the target maximum current and other engineering constraints, one approach to achieving stronger gradients was to increase the wire-width-based FOM β_J during the coil design process.

To enhance the wire-width-based figure of merit β_J for the nonlinear coil design, the maximum norm of the current density $\vec{J}$ needed to be reduced while maintaining the average gradient strength of the encoding fields across the ROI, as described by Eq. (1). A successful approach [18, 19] to reducing the maximum norm of the electric current density $\vec{J}$ on a current-carrying surface Γ involved minimizing the p-norm ($\|J\|_p := (\int_\Gamma |\vec{J}|^p \mathrm{d}\Gamma)^{1/p} (p > 2)$) of the surface current density, which converges to the maximum norm of $\vec{J}$ when p approaches infinity. Moreover, coil power dissipation was incorporated as a regularization term in the optimization problem to make the resulting coil layout smooth [15].

The second requirement was to control y-axis gradient variation, possibly enhancing the diagnostic value of the diffusion weighting close to the chest wall. The third requirement was that the encoding field generated by a non-linear breast coil have a nearly constant gradient magnitude within each coronal slice [13]. This requirement will allow the resulting coil to be employed for diffusion weighting within each coronal slice in a manner similar to the currently established protocols that rely on linear gradients [20]. Finally, the electromagnetic force and torque on the coil also needed to be controlled during the design process.

Based on the above requirements, the following optimization problem was proposed:

$$\min_{\psi} \sqrt{P(\psi)} + \alpha_J \|\vec{J}(\psi)\|_p,$$

$$\text{subject to } \frac{1}{k} \sum_{\vec{x}_i \in \mathrm{ROI}} |\nabla B_z(\psi, \vec{x}_i)| \geq C_g, \tag{2}$$

$$D_y := \left(\sum_{\vec{x}_i \in \mathrm{ROI}} \left(\frac{\partial |\nabla B_z(\psi, \vec{x}_i)|}{\partial y} \right)^2 \right)^{\frac{1}{2}} \leq k C_y C_g, \tag{3}$$

$$D_s := \left(\sum_{\vec{x}_i \in \mathrm{ROI}} \left(\frac{\partial |\nabla B_z(\psi, \vec{x}_i)|}{\partial x} \right)^2 + \left(\frac{\partial |\nabla B_z(\psi, \vec{x}_i)|}{\partial z} \right)^2 \right)^{\frac{1}{2}} \leq k C_s C_g,$$

$$|F_x| := \left| \int_\Gamma B_0 J_y(\psi) \mathrm{d}\Gamma \right| \leq F_{\max} C_g,$$

$$|F_y| := \left| -\int_\Gamma B_0 J_x(\psi) \mathrm{d}\Gamma \right| \leq F_{\max} C_g,$$

$$|M_x| := \left| \int_\Gamma B_0 J_x(\psi) z \mathrm{d}\Gamma \right| \leq M_{\max} C_g,$$

$$|M_y| := \left| \int_\Gamma B_0 J_y(\psi) z \mathrm{d}\Gamma \right| \leq M_{\max} C_g,$$

$$|M_z| := \left| -\int_\Gamma B_0 \left(J_x(\psi) x + J_y(\psi) y \right) \mathrm{d}\Gamma \right| \leq M_{\max} C_g. \tag{4}$$

Here, ψ denotes the scalar piecewise-linear stream function [21] of the electric current density vector $\vec{J}(\psi) := (J_x(\psi), J_y(\psi), J_z(\psi))^T$ and $\vec{J}(\psi) = \nabla \times (\psi \vec{n})$ on a current-carrying surface Γ (Fig. 1) with a normal unit vector $\vec{n}$. $P(\psi) := \|\vec{J}(\psi)\|_2^2 / (\tau \sigma_e)$ is power dissipated by the coil, where τ and σ_e indicate the thickness and the electrical conductivity of the surface Γ, respectively. The vectors $\vec{x}_i = (x_i, y_i, z_i)^T$, $i = 1, \ldots, k$, denote the positions of the test points in the ROI. The z-component of the magnetic field, $B_z(\psi, \vec{x}_i)$, is generated by $\vec{J}(\psi)$ and evaluated at $\vec{x}_i$ using the Biot–Savart law.

In this problem, $D_s := \left(\sum_{\vec{x}_i \in \mathrm{ROI}} (\partial |\nabla B_z(\psi, \vec{x}_i)| / \partial x)^2 + (\partial |\nabla B_z(\psi, \vec{x}_i)| / \partial z)^2 \right)^{\frac{1}{2}}$ indicates the per-slice constraint, which is used to homogenize the gradient strength of B_z within each of the coronal slices, as proposed in our previous work [13]. Compared to the previous optimization formulation in [13], a new constraint for $D_y := \left(\sum_{\vec{x}_i \in \mathrm{ROI}} (\partial |\nabla B_z(\psi, \vec{x}_i)| / \partial y)^2 \right)^{\frac{1}{2}}$ is introduced to control the gradient variation along the y-axis.

In this problem, F_x and F_y indicate x- and y-components of the net force on the coil, respectively, in the presence of a main magnetic field B_0 along z-direction. In the examples of this manuscript, the main field B_0 is assumed to be homogeneous with the strength of 3 T since the built prototype of the designed coil will be used close to the isocenter of the main magnet generating field B_0. Therefore, the constraints of F_x and F_y are naturally satisfied and can be ignored during the optimization of Problem (2). M_x, M_y and M_z denote x-, y- and z-components of the magnetic torque experienced by the coil, respectively. $F_{\max}$ and $M_{\max}$ are two given positive constants with the unit of N and N·m in order to set a limitation of the total force and the total magnetic torque, respectively.

The optimization problem also contains four positive tuning parameters: the current density regularization weight α_J, the minimum average gradient strength threshold C_g, the intra-slice gradient uniformity parameter C_s and the anterior–posterior gradient variation parameter C_y. Physically, C_s limits the variation of$|\nabla B_z|$ within each coronal slice, while C_y limits the variation of $|\nabla B_z|$ along the anterior—posterior direction. A smaller value of C_s and C_y enforces stricter spatial uniformity of the encoding gradient. However, considering that the stream function ψ in the current optimization problem is linearly dependent on C_g, we only need to consider three tuning parameters α_J, C_s and C_y.

In order to guarantee that resulting wire patterns are closed on the current-carrying surface Γ, all values of the stream function ψ must remain constant on each closed boundary of Γ [21]. Moreover, ψ is typically specified as a given constant, such as 0, at one point in Γ or on one closed boundary of Γ to avoid the existence of infinitely many solutions of Problem (2). Without this requirement for any stream function ψ, which is a solution of Problem (2), ψ plus any constant is also a solution of Problem (2). As shown in Fig. 1, the current-carrying surface Γ has only one boundary and ψ on the boundary is set to 0 in all subsequent numerical examples.

Three other performance measures

In addition to the wire-width-based figure of merit β_J, the resistive FOM β_P, inductive FOM β_W and the coefficient of variation CV_D of the coil efficiency η over the domain D are used to assess and compare different breast coil designs. The formulae for β_P, β_W [13] and CV_D are defined as follows:

$$\beta_P := \frac{\sum_{\vec{x}_i \in \mathrm{ROI}} |\nabla B_z(\psi, \vec{x}_i)|}{k\sqrt{P(\psi)}}, \tag{5}$$

$$\beta_W := \frac{\sum_{\vec{x}_i \in \mathrm{ROI}} |\nabla B_z(\psi, \vec{x}_i)|}{k\sqrt{W(\psi)}}, \tag{6}$$

$$\mathrm{CV}_D := \frac{\mathrm{std}(\eta)_D}{\mathrm{mean}(\eta)_D}. \tag{7}$$

Here, $W(\psi) := \frac{\mu_0}{8\pi} \int_\Gamma \int_{\Gamma'} \frac{\vec{J}(\psi(\vec{x})) \cdot \vec{J}(\psi(\vec{x}'))}{|\vec{x}-\vec{x}'|} \mathrm{d}\Gamma' \mathrm{d}\Gamma$ [22] indicates coil magnetic energy and μ_0 denotes the magnetic constant of $4\pi \times 10^{-7}$ H/m. The $\mathrm{std}(\eta)_D$ and $\mathrm{mean}(\eta)_D$ denote the standard deviation and mean value of the coil efficiency η over the domain D, respectively.

As shown in Eq. (5), β_P, with the unit of $\mathrm{T/(m \cdot A \cdot \Omega^{1/2})}$, is defined as the average gradient strength of the encoding field over the ROI divided by the square root of the power dissipation. For a given dissipated power, a larger β_P indicates a higher average gradient strength. Similarly, as presented in Eq. (6), β_W, with the unit of $\mathrm{T/(m \cdot A \cdot H^{1/2})}$, is described as the average gradient strength of the encoding field over the ROI divided by the square root of the stored magnetic energy. Thus, for given magnetic energy, a larger β_W implies a higher average gradient strength and better coil performance. Finally, as described in Eq. (7), the coefficient of variation CV_D, with no unit, is employed to assess the spatial uniformity of the gradient strength over a specified domain D. In this work, the domain D represents either an individual coronal slice ($D = s$) or the entire ROI ($D = ROI$).

Numerical optimization procedure

In order to select a suitable breast coil, Problem (2) with different values of α_J, C_s and C_y was solved to obtain different non-linear coil layouts. In order to obtain suitable values of the tuning parameters for a non-linear breast coil design comparable to its corresponding linear one, the whole procedure of selecting the tuning parameters has been divided into three steps. In the first step, a linear breast coil is designed using the method described in [13] when the target field B_z^* is provided. Here, B_z^* is specified as linear G_z with the gradient strength of 50 mT/m, as recommended in [13]. For the resulting linear coil, D_y and D_s indicated by D_y^l and D_s^l were calculated using Eqs. (3) and (4), respectively. In the examples, C_g was specified to be $\left(\sum_{\vec{x}_i \in \mathrm{ROI}} (|\nabla B_z(\psi, \vec{x}_i)|)^2\right)^{\frac{1}{2}} / k$, where B_z denotes the magnetic field generated by the resulting linear coil with a target gradient strength of 50 mT/m. The two constants C_y^l and C_s^l were defined by $D_y^l/k/C_g$ and $D_s^l/k/C_g$, respectively, which were used for next steps.

Second, the parameter C_s was selected from a list that decreases proportionally starting from C_s^l. For each given C_s, Problem (2) with $\alpha_J = 0$ and without the constraint (3) was solved to obtain a non-linear breast coil. For the resulting non-linear coil, D_y indicated by D_y^m was calculated using Eq. (3) and the constant C_y^m was defined by $D_y^m/k/C_g$. In the examples, C_s was taken from $[C_s^l\ C_s^l/2.5\ C_s^l/5]$ and the resulting stream function from the first step was used as an initial value of the current problem. Finally, the parameters C_y and α_J were taken from the intervals $[C_y^l\ C_y^m]$ and $[0\ \alpha_J^m]$ with the steps C_y^s and α_J^s, respectively. In the examples, α_J^m, C_y^s and α_J^s were specified as to be 8e-3, $(C_y^m - C_y^l)/10$ and 2.5e−4, respectively.

After generating the set of candidate nonlinear coil layouts, a suitable design was selected for prototype fabrication based on a defined set of performance criteria. First, the parameter C_s was determined based on the coefficient of variation, CV_s, evaluated on representative coronal slices. Specifically, C_s was chosen such that the resulting design exhibits a CV_s comparable to or lower than the corresponding $\mathrm{CV}_{\mathrm{ROI}}$ of the conventional linear G_z coil. This criterion ensures that the nonlinear encoding field maintains intra-slice gradient uniformity comparable to that of the linear reference design.

With C_s fixed, the remaining design was selected according to the intended performance trade-offs. In particular, if improved gradient uniformity along the y-axis is prioritized, a design with a lower $\mathrm{CV}_{\mathrm{ROI}}$ is recommended. If higher average coil efficiency $\bar{\eta}$ is the primary objective, a design with a larger β_J should be selected under a fixed minimum wire-width constraint. Similarly, reduced magnetic energy can be achieved by choosing a design with a larger β_W at a fixed $\bar{\eta}$, whereas lower power dissipation can be obtained by selecting a design with a larger β_P under the same efficiency constraint.

It is worth noting that these performance metrics are independent of the discretization of the coil layout, i.e., they do not depend on the number of contour levels used in the stream-function-to-wire conversion.

Finally, high gradient slew rates generally require low coil inductance. To evaluate the inductance of a discretized coil, the operating current must first be specified. After obtaining the optimal stream function ψ on Γ, the operating current is determined according to [21] as $(\psi_{\max} - \psi_{\min})/NC$, where NC denotes the total number of contours. A smaller NC leads to a lower coil inductance but requires a higher operating current to satisfy the gradient-strength constraint C_g. Conversely, a larger NC increases inductance but reduces the required operating current for the same gradient target.

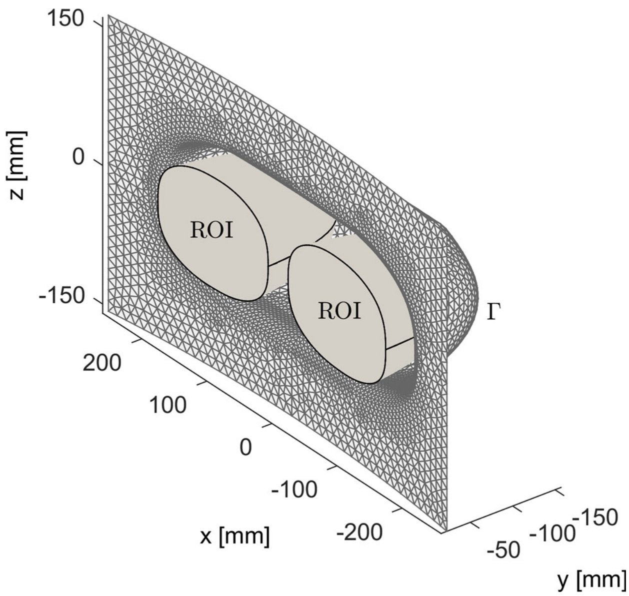

Fig. 1 Geometries of the ROI and current-carrying surface Γ

Therefore, NC must be selected to balance gradient strength and slew-rate performance.

Coil geometry and physical parameters

Volumes and surfaces were designed using the 3D design suite Inventor (Autodesk, San Rafael, CA, USA). For the examples shown, the current-carrying surface Γ (Fig. 1) was designed to have one volume, large enough to house an additional radio frequency (RF) transceiver coil, with enough space to fit the necessary electrical components. The RF coil has two separate independent cups for each breast, which are the ROIs of the coil design (Fig. 1). The volume of each ROI was chosen to include at least 85% of the female population. Each ROI extends 160 mm × 125 mm × 120 mm (horizontal × vertical × longitudinal), resulting in a net volume of 1.44L. The current carrying surface consists of a top part along the horizontal direction, which is slightly curved for patient comfort and has a rectangular base shape of 520 mm × 320 mm (horizontal × longitudinal). The main opening is 290 mm × 152 mm (horizontal × longitudinal) wide and has a depth between 126 mm and 136 mm (sagittal) from the top of the curved surface. In Autodesk Inventor, the bridge curve and loft functions were used to design the target volumes, the current carrying surface, and the RF carrier structure. The electrical conductivity was set as $\sigma_e = 5.998 \times 10^4$ S/mm. The conductor thickness τ and minimum wire width were set to 3 mm and 3.5 mm, respectively, to ensure sufficient current-carrying capacity of 650 A, based on our prior fabrication experience. $F_{\max}$ and $M_{\max}$ are specified as 1×10^{-4} N and 1×10^{-4} N·m, respectively, to limit the total net magnetic force and torque of a designed coil.

Prototype and field map measurement

One optimal stream function was selected and transformed to a discretized wire pattern using the automatized algorithm [23]. A prototype of the discretized coil was built in-house [24, 25]. In order to demonstrate the validity of the design method, an initial field map of the prototype was measured using a modified 2D multi-slice spoiled gradient echo sequence (GRE) similar to [26]. The modified sequence consists of two parts. The first part is a standard 2D multi-slice spoiled GRE sequence and the second part is the same sequence with an extra gradient pulse on the prototype (0.5 ms, 2 A). The gradient pulse parameters were chosen to avoid wrapping of the resulting phase map. The imaging parameters were: TE = 7 ms, TR = 10 ms, flip angle = 20 degree, in-plane resolution = 4 mm, field of view = 320 × 320 mm, slice thickness = 4 mm and 55 slices. All the measured data were acquired using a water phantom and a 3T Achieva MRI system (Philips, Best, The Netherlands).

Results

This section is organized into four subsections. The first subsection presents a comparison between a linear gradient coil and two non-linear designs—one without and one with the proposed y-axis gradient variation constraint. The second "Performance impact of different tuning parameters in non–linear coil designs" investigates the influence of key tuning parameters (C_s, C_y, and α_J) on multiple figures of merit, highlighting performance trade-offs. The third "Non-linear coil designs with the minimum width of 3.5 mm" evaluates a series of non-linear designs that satisfy a minimum wire width constraint of 3.5 mm, focusing on gradient uniformity and layout complexity. Finally, "Prototype and field map measurement" reports on the experimental validation of a prototype coil, including comparisons between measured and simulated magnetic fields.

Comparison of linear and non-linear coils

Table 1 presents a quantitative comparison between a linear G_z coil, an old non-linear gradient coil, and a new non-linear gradient coil, all designed using the same $C_s = 0.159$. The old non-linear coil was optimized without the y-axis gradient variation constraint (3), as described in [13], while the new non-linear coil incorporates this additional constraint to improve gradient uniformity along the anterior–posterior direction.

Compared to the linear coil, both non-linear designs achieve substantially higher encoding efficiency. Specifically, the average coil efficiency $\bar{\eta}$ of the old and new non-linear coils is approximately 2.79 and 2.35 times higher than

Table 1 Performance comparison of the linear gradient coil, the old and new non-linear gradient coils with the same intra-slice gradient uniformity parameter C_s

Properties	Linear G_z coil	Old non-linear coil	New non-linear coil
C_s	0.159	0.159	0.159
C_y	0.119	–	0.119
$D_y/k/C_g$	0.119	0	0.119
α_J	–	0	0
Number of contours	26	26	26
Current I [A]	65.6	23.6	27.9
$\eta := \lvert\nabla B_z\rvert/I$ [mT/m/A]	[0.45,1.34]	[0.139, 5.37]	[0.366,3.21]
$\bar{\eta}$ =mean(η) [mT/m/A]	0.783	2.18	1.84
σ_η :=std(η) [mT/m/A]	0.08	1.23	0.666
$\mathrm{CV_{ROI}} := \sigma_\eta/\bar{\eta}$	0.102	0.563	0.362
β_J [μT/A]	1.4	5.3	5.95
β_P [mT/(m·A·$\Omega^{1/2}$)]	4.2	11.6	10.2
β_W [T/(m·A·$H^{1/2}$)]	0.097	0.257	0.219
Coil inductance [μH]	131	145	142
Coil resistance [mΩ]	34.8	35.2	32.6
max($\lvert M_x\rvert, \lvert M_y\rvert, \lvert M_z\rvert$) [N·m]	1.0e−4	1.0e−4	1.0e−4
$w_{\min}$ [mm]	1.79	2.43	3.23

The old non-linear coil was designed without incorporating the new constraint (3), as described in the previous work [13]. In contrast, the new non-linear coil was obtained by including the y-axis gradient variation constraint (3) in the optimization process

Table 2 Performance comparison of non-linear gradient coils designed with an intra-slice gradient uniformity parameter of $C_s = 0.159$

Properties	Non-linear coils when $C_s = 0.159$			
Case	1	2	3	4
C_y	0.119	0.136	0.153	0.16
α_J	6.38e−3	6.69e−3	7.44e−3	3.09e−3
Number of contours	32	30	28	26
Current I [A]	25.8	25.2	25	25.4
$\eta := \lvert\nabla B_z\rvert/I$ [mT/m/A]	[0.47,3.38]	[0.406,3.54]	[0.343,3.92]	[0.292,3.99]
$\bar{\eta}$ =mean(η) [mT/m/A]	1.99	2.04	2.06	2.02
σ_η :=std(η) [mT/m/A]	0.65	0.72	0.793	0.825
$\mathrm{CV_{ROI}} := \sigma_\eta/\bar{\eta}$	0.327	0.353	0.386	0.408
β_J [μT/A]	6.96	7.14	7.2	7.08
β_P [mT/(m·A·$\Omega^{1/2}$)]	9.71	10.2	10.4	10.8
β_W [T/(m·A·$H^{1/2}$)]	0.208	0.219	0.225	0.232
Coil inductance [μH]	182	174	167	151
Coil resistance [mΩ]	41.9	40.2	38.9	35.1
max($\lvert M_x\rvert, \lvert M_y\rvert, \lvert M_z\rvert$) [N·m]	1.0e−4	1.0e−4	1.0e−4	1.0e−4
$w_{\min}$ [mm]	3.5	3.5	3.5	3.5

that of the linear coil, respectively. The wire-width-based figure of merit β_J improves by factors of approximately 3.78 (old non-linear) and 4.25 (new non-linear) over the linear design. These increases demonstrate the advantage of non-linear encoding in producing stronger local gradients per unit current.

However, this gain in efficiency comes with increased spatial non-uniformity. Compared to the linear coil, the coefficient of variation $\mathrm{CV_{ROI}}$ for the old non-linear coil increases by a factor of approximately 5.5. By including the C_y constraint in the new non-linear coil, $\mathrm{CV_{ROI}}$ shows a 35.7% decrease compared to the old design. Moreover, the minimum coil efficiency near the chest wall also improves significantly. Compared to the old non-linear coil, the minimum value of η in the new non-linear coil increases by a factor of approximately 2.63.

Table 3 Performance comparison of non-linear gradient coils designed with an intra-slice gradient uniformity parameter of C_s = 0.0636

Properties	Non-linear coils when C_s = 0.0636			
Case	1	2	3	4
C_y	0.119	0.132	0.16	0.169
α_J	1.88e−3	4.88e−3	4.63e−3	4.88e−3
Number of contours	28	28	26	26
Current I [A]	31	30.4	31	31.1
$\eta := \|\nabla B_z\|/I$ [mT/m/A]	[0.651, 2.83]	[0.625, 3.15]	[0.521, 3.62]	[0.519, 3.63]
$\bar{\eta}$ =mean(η) [mT/m/A]	1.66	1.69	1.65	1.65
σ_η :=std(η) [mT/m/A]	0.503	0.566	0.671	0.674
$\mathrm{CV_{ROI}} := \sigma_\eta/\bar{\eta}$	0.303	0.335	0.406	0.408
β_J [μT/A]	5.81	5.91	5.79	5.79
β_P [mT/(m·A·$\Omega^{1/2}$)]	8.61	8.7	9.04	9.03
β_W [T/(m·A·$H^{1/2}$)]	0.179	0.182	0.19	0.19
Coil inductance [μH]	172	172	151	151
Coil resistance [mΩ]	37.2	37.7	33.5	33.5
max($\|M_x\|, \|M_y\|, \|M_z\|$) [N·m]	1.0e−4	1.0e−4	1.0e−4	1.0e−4
$w_{\min}$ [mm]	3.5	3.5	3.5	3.5

Table 4 Performance comparison of non-linear gradient coils designed with an intra-slice gradient uniformity parameter of C_s = 0.0318

Properties	Non-linear coils when C_s = 0.0318				
Case	1	2	3	4	5
C_y	0.119	0.135	0.16	0.16	0.182
α_J	5.49e−3	4.46e−3	1.26e−3	7.13e−3	4.44e−3
Number of contours	32	30	26	28	26
Current I [A]	34.4	34.5	36.1	34.7	35.6
$\eta := \|\nabla B_z\|/I$ [mT/m/A]	[0.729, 2.64]	[0.671, 2.85]	[0.562, 3.06]	[0.593, 3.22]	[0.523, 3.43]
$\bar{\eta}$ =mean(η) [mT/m/A]	1.49	1.49	1.42	1.48	1.44
σ_η :=std(η) [mT/m/A]	0.453	0.511	0.576	0.599	0.652
$\mathrm{CV_{ROI}} := \sigma_\eta/\bar{\eta}$	0.304	0.344	0.406	0.404	0.452
β_J [μT/A]	5.22	5.21	4.98	5.19	5.05
β_P [mT/(m·A·$\Omega^{1/2}$)]	7.12	7.51	8.17	7.86	8.16
β_W [T/(m·A·$H^{1/2}$)]	0.152	0.159	0.171	0.166	0.172
Coil inductance [μH]	192	175	138	158	140
Coil resistance [mΩ]	43.9	39.2	30.3	35.5	31.2
max($\|M_x\|, \|M_y\|, \|M_z\|$) [N·m]	1.0e−4	1.0e−4	1.0e−4	1.0e−4	1e−4
$w_{\min}$ [mm]	3.5	3.5	3.5	3.5	3.5

Although the new non-linear coil exhibits slightly lower $\bar{\eta}$ and performance metrics β_P and β_W than the old non-linear version (decreased by factors of approximately 1.18 and 1.17, respectively), it achieves a markedly better trade-off between efficiency and gradient uniformity. Furthermore, the new coil features a larger minimum wire width $w_{\min}$ (3.23 mm vs. 2.43 mm), which is beneficial for fabrication and thermal management.

Performance impact of different tuning parameters in non-linear coil designs

Figure 2a–c illustrate the variation of β_J with respect to different values of C_y and α_J for $C_s = 0.159$, 0.0636, and 0.0318, respectively. As observed, β_J decreases as C_s decreases, given fixed values of C_y and α_J. Specifically, compared to $C_s = 0.159$, the mean values of β_J for $C_s = 0.0636$ and $C_s = 0.0318$ are reduced by factors of approximately 1.22 and 1.4, respectively.

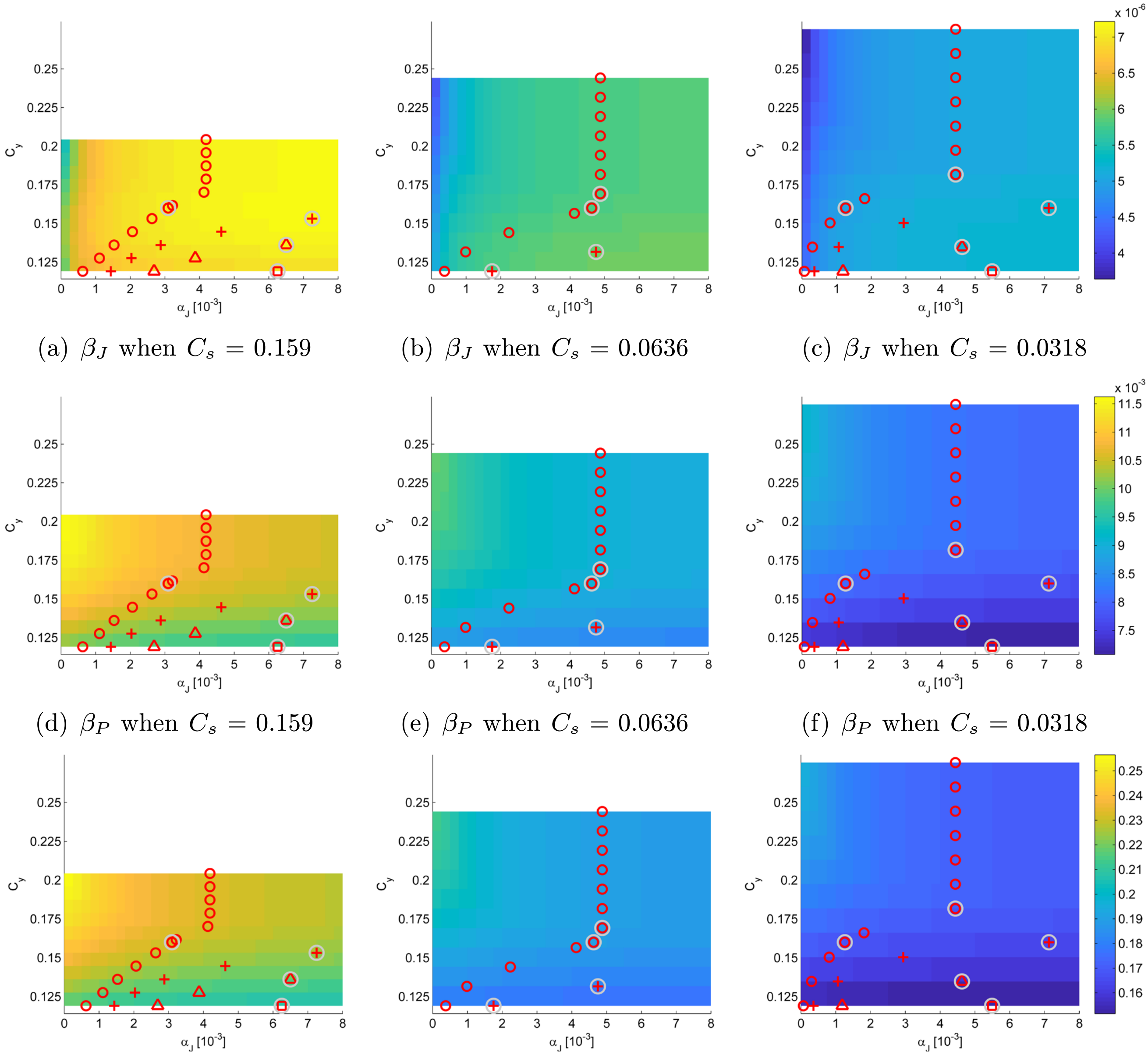

(a) β_J when $C_s = 0.159$ (b) β_J when $C_s = 0.0636$ (c) β_J when $C_s = 0.0318$

(d) β_P when $C_s = 0.159$ (e) β_P when $C_s = 0.0636$ (f) β_P when $C_s = 0.0318$

(g) β_W when $C_s = 0.159$ (h) β_W when $C_s = 0.0636$ (i) β_W when $C_s = 0.0318$

Fig. 2 Figures of merit β_J, β_P and β_W for intra-slice gradient uniformity parameters of $C_s = 0.159$ (**a**, **d**, **g**), 0.0636 (**b**, **e**, **h**) and 0.0318 (**c**, **f**, **i**). Red markers (circles, crosses, triangles, and squares) denote 26, 28, 30, and 32 wire turns, respectively, where the number of turns in each case is determined by the minimum wire width constraint of 3.5 mm. Performance parameters corresponding to the points marked by gray circles are detailed in Tables 2, 3, and 4. Subfigures **a–c**, **d–f**, and **g–i** each share a common color bar

For a given C_s, β_J increases rapidly at lower values of α_J, followed by a more gradual rise as α_J increases, for fixed C_y. When $C_s = 0.159$, β_J initially increases with C_y for a fixed α_J, but then slightly decreases or levels off. This behavior suggests that optimal average coil efficiency $\bar{\eta}$ is achieved at higher α_J combined with a moderately increased C_y, for a given minimum wire width. In contrast, when $C_s = 0.0636$ and 0.0318, β_J tends to decrease as C_y increases at a fixed α_J, and subsequently either slightly declines further or remains stable. This indicates that, in these cases, optimal coil efficiency $\bar{\eta}$ is achieved at larger α_J and lower C_y, highlighting a shift in the optimal parameter regime as C_s decreases.

The second and third rows of Fig. 2 present the trends of β_P and β_W, respectively. Similar to β_J, both β_P and β_W decrease with decreasing C_s, for fixed C_y and α_J. Specifically, the mean values of β_P for $C_s = 0.0636$ and 0.0318 are reduced by factors of approximately 1.17 and 1.32, respectively, compared to $C_s = 0.159$. Likewise, the mean values

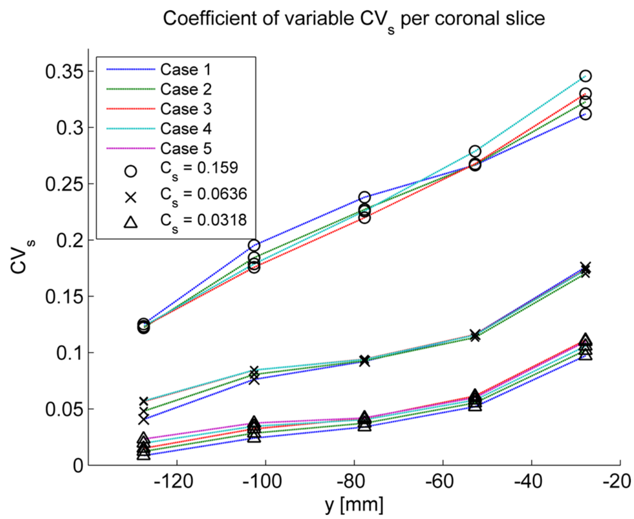

Fig. 3 Coefficients of variable per coronal slice. For intra-slice gradient uniformity parameters of C_s = 0.159, 0.0636 and 0.0318, the corresponding tuning and performance parameters for different cases (i.e., different values of the current density regularization weight, (α_J), or the anterior–posterior gradient variation parameter, (C_y)) are presented in Tables 2, 3 and 4, respectively. C_s = 0.159 and C_s = 0.0636 have four different cases and C_s = 0.0318 has five cases

of β_W decrease by factors of 1.2 and 1.34, respectively. For a given C_s, both β_P and β_W exhibit a decreasing trend with increasing α_J at fixed C_y. Additionally, as C_y increases for fixed α_J, both β_P and β_W initially decrease and then either slightly decline further or stabilize. These trends suggest that optimal values of β_P and β_W are generally achieved at higher α_J and moderately elevated C_y.

Non-linear coil designs with the minimum width of 3.5 mm

Figure 2 also highlights the points with a minimum width of 3.5 mm. The red points delineated by circles, crosses, triangles and rectangles represent wire turn numbers of 26, 28, 30 and 32, respectively. Some points with relatively high β_J values are marked with gray circles. Their specific performance metrics for $C_s = 0.159, 0.0636$, and 0.0318 are presented in Table 2, 3 and 4 respectively.

Table 2 compares the performance of four non-linear gradient coil designs optimized with $C_s = 0.159$, while varying the y-axis gradient variation constraint C_y. For each design, the parameter α_J was individually adjusted to ensure that the minimum wire width constraint of 3.5 mm was satisfied. As C_y increases from 0.119 to 0.16, a clear deterioration in gradient uniformity is observed. The standard deviation of coil efficiency σ_η and the coefficient of variation CV_{ROI} over the ROI increase by factors of 1.27 and 1.25, respectively. In contrast, the average coil efficiency $\bar{\eta}$ remains relatively stable across the range of C_y. An improvement in $\bar{\eta}$ by a factor of approximately 1.04 is observed as C_y increases from 0.119 to 0.153. However, when C_y increases further from 0.153 to 0.16, $\bar{\eta}$ decreases by a factor of 1.02. These observations suggest that a moderate increase in C_y can slightly enhance average efficiency, but at the cost of reduced gradient uniformity across coronal slices.

Table 3 compares the performance of four non-linear gradient coil designs optimized with $C_s = 0.0636$, while varying the y-axis gradient variation constraint C_y. As C_y increases from 0.119 to 0.169, a progressive deterioration in gradient uniformity is again observed. The standard deviation σ_η and the coefficient of variation CV_{ROI} over the ROI increase by factors of approximately 1.34 and 1.35, respectively. Meanwhile, the average coil efficiency $\bar{\eta}$ remains relatively stable. A slight improvement is seen as C_y increases from 0.119 to 0.132, followed by a marginal decrease as C_y increases further to 0.169. The overall variation in $\bar{\eta}$ across this range remains within a factor of approximately 1.02, indicating that relaxing C_y has minimal impact on efficiency in this regime.

Table 4 summarizes the performance of five non-linear gradient coil designs optimized with $C_s = 0.0318$, while varying the constraint C_y. As C_y increases from 0.119 to 0.182, a notable decline in gradient uniformity is observed. The standard deviation σ_η and coefficient of variation CV_{ROI} over the ROI increase by factors of approximately 1.44 and 1.49, respectively. These trends confirm that relaxing the C_y constraint leads to increasing heterogeneity in the encoding gradient along the y-axis. Unlike the cases with higher C_s, the average coil efficiency $\bar{\eta}$ does not exhibit a clear improvement with increasing C_y. Across the full range tested, the variation in $\bar{\eta}$ remains within a factor of approximately 1.05, indicating limited sensitivity of average efficiency to changes in C_y when strong C_y is applied.

Table 4 also includes two designs with $C_y = 0.16$, which differ in their values of α_J (1.26e−3 and 7.13e−3). Compared to the lower α_J, both $\bar{\eta}$ and σ_η increase by a factor of approximately 1.04 in the higher α_J case. Interestingly, CV_{ROI} over the ROI slightly decreases by a factor of 1.003, suggesting that CV_{ROI} may serve as a more stable and robust indicator of gradient uniformity than σ_η. Additionally, the design with higher α_J requires an increased number of contours to maintain the minimum wire width of 3.5 mm. This increase in coil-layout complexity may present more challenges in coil fabrication and winding.

Tables 2, 3, and 4 also show that these optimized coils all possess an inductance of less than 200 μH, representing more than a 5-fold reduction compared to a conventional whole-body gradient coil [7]. These results suggest that a higher slew rate can be achieved. Moreover, the maximum components of the torque vector are exceptionally small (on the order of 1e−4 ·m), indicating that the coil layouts are

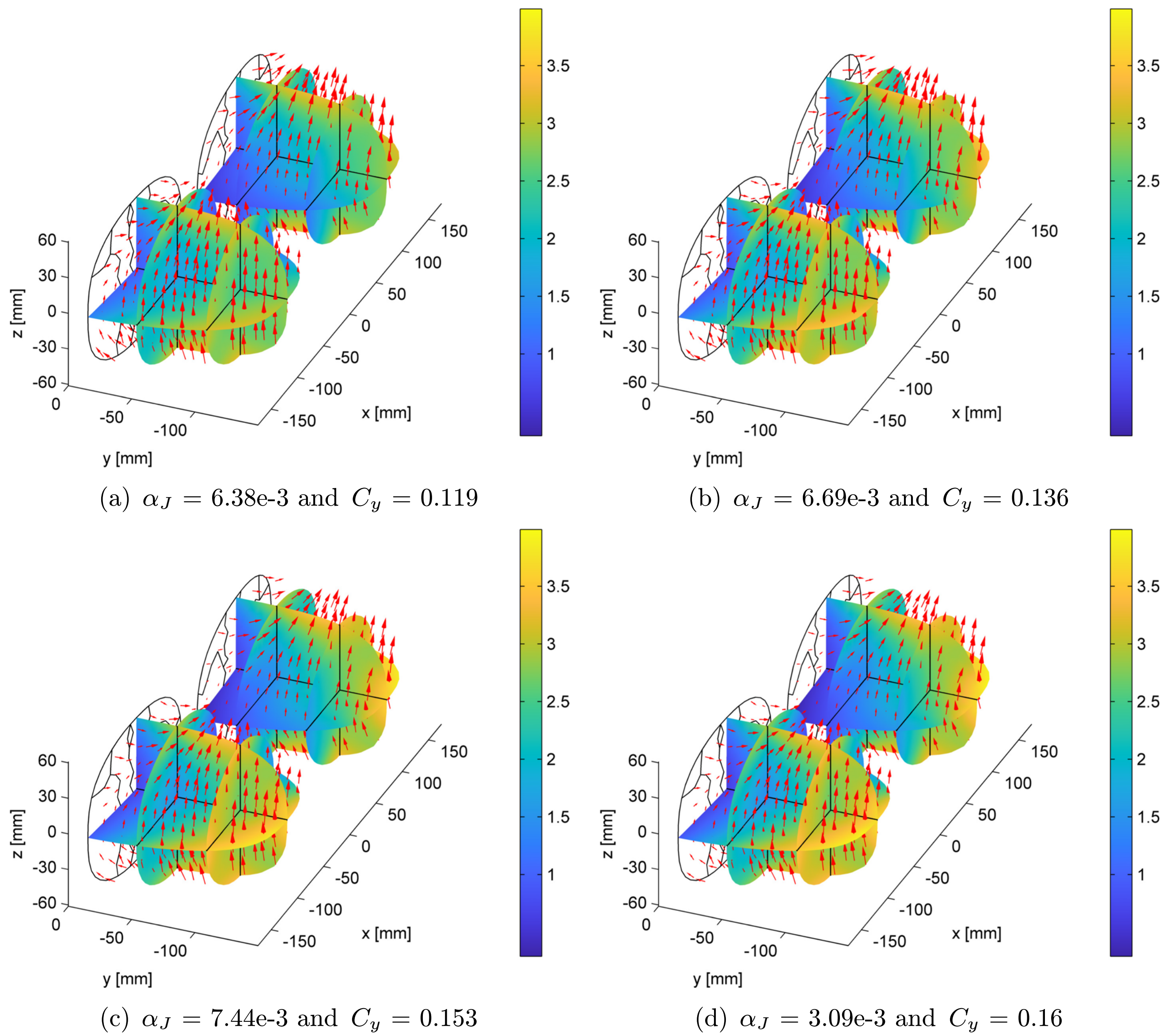

(a) α_J = 6.38e-3 and C_y = 0.119

(b) α_J = 6.69e-3 and C_y = 0.136

(c) α_J = 7.44e-3 and C_y = 0.153

(d) α_J = 3.09e-3 and C_y = 0.16

Fig. 4 Spatial distributions of coil efficiency η [mT/m/A] (color map) for different values of the current density regularization weight, α_J, and the anterior–posterior gradient variation parameter, C_y, with the intra-slice gradient uniformity parameter fixed at $C_s = 0.159$. The gradient vectors of the magnetic field B_z per unit current are indicated by red arrows

nearly mechanically balanced within a constant main magnetic field.

Figure 3 shows the coefficient of variation per coronal slice, denoted as CV_s, as a function of the slice position y, spanning from anterior ($y = -128$ mm) to posterior region ($y = -27.9$ mm) of the ROI. Several different nonlinear coil design cases are presented for $C_s = 0.159$, 0.0636, and 0.0318, represented by circular, cross and triangular markers, respectively. From case 1 to case 5, the corresponding value of C_y increases or remains constant.

For all values of C_s, the average value of CV_s increases progressively with slice position, from anterior ($y = -128$ mm) to posterior ($y = -27.9$ mm). This trend reflects increasing intra-slice gradient non-uniformity in slices closer to the chest wall. Specifically, for $C_s = 0.159$, the average CV_s rises from 0.124 in the anterior slice to 0.328 in the most posterior slice. For $C_s = 0.0636$, the corresponding values increase from 0.051 to 0.173, and for $C_s = 0.0318$, from 0.016 to 0.105. These results confirm that stronger per-slice constraints (i.e., lower C_s) result in reduced intra-slice variation over the ROI.

Considering that the designed linear coil exhibits a coefficient of variation of 0.102 over the ROI, as shown in Table 1, the nonlinear designs with $C_s = 0.0318$ may offer compara-

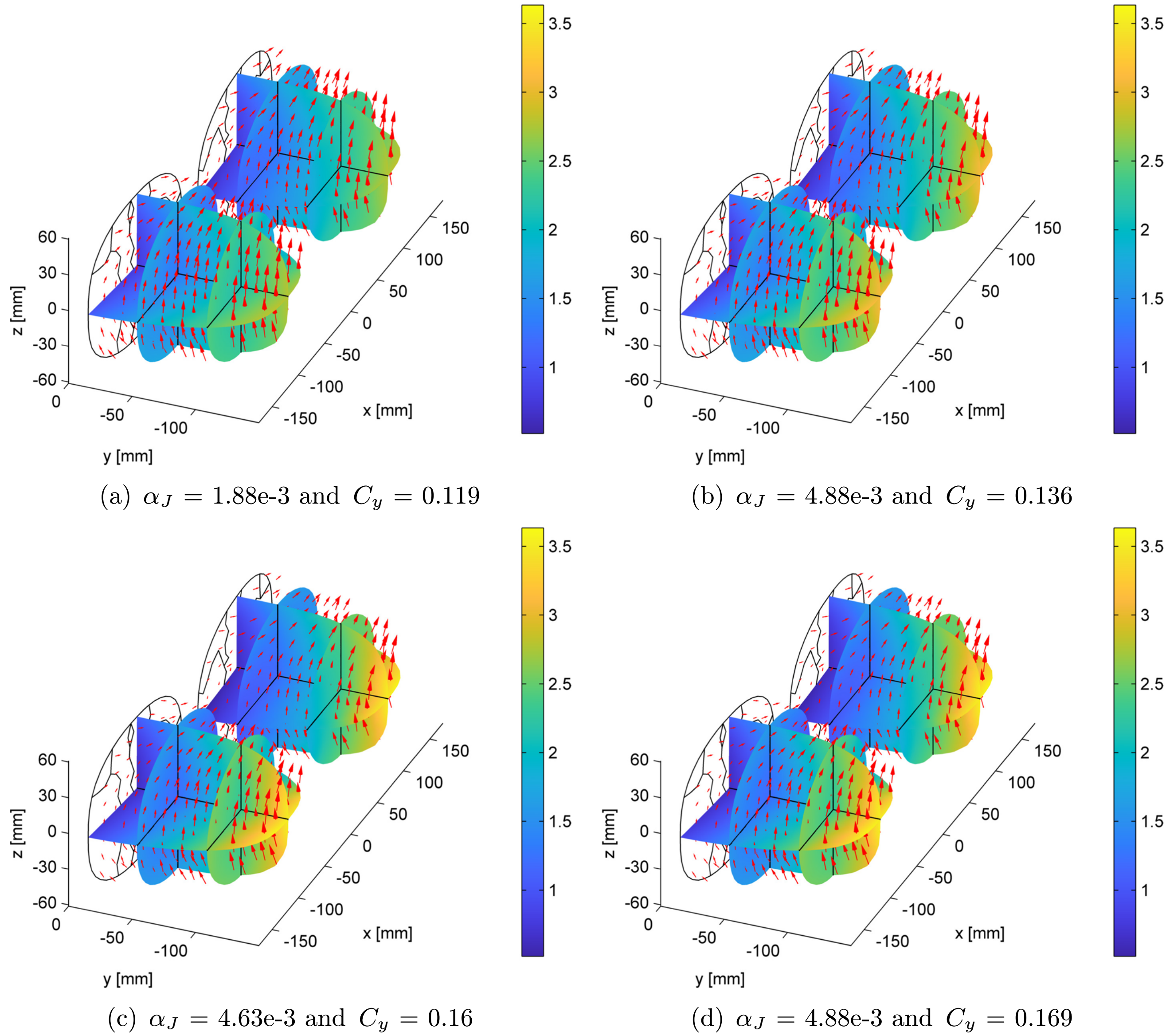

(a) $\alpha_J = 1.88\text{e-}3$ and $C_y = 0.119$

(b) $\alpha_J = 4.88\text{e-}3$ and $C_y = 0.136$

(c) $\alpha_J = 4.63\text{e-}3$ and $C_y = 0.16$

(d) $\alpha_J = 4.88\text{e-}3$ and $C_y = 0.169$

Fig. 5 Spatial distributions of coil efficiency η [mT/m/A] (color map) for different values of the current density regularization weight, α_J, and the anterior–posterior gradient variation parameter, C_y, with the intra-slice gradient uniformity parameter fixed at $C_s = 0.0636$. The gradient vectors of the magnetic field B_z per unit current are indicated by red arrows

ble or even superior gradient uniformity within each coronal slice, making them a favorable choice when aiming to match the gradient homogeneity achieved by linear gradient coils.

For a given C_s, Fig. 3 also illustrates the effect of C_y on the coefficient of variation CV_s. The maximum standard deviation of CV_s across all coronal slices is 0.0142 for $C_s = 0.159$, 0.008 for $C_s = 0.0636$, and 0.006 for $C_s = 0.0318$. However, in contrast to the trend observed for CV_{ROI} (as shown in Tables 2, 3, and 4), increasing C_y does not consistently lead to an increase in CV_s at each individual slice.

Figures 4, 5 and 6 show the distribution of coil efficiency η over the ROI for the tuning parameters of C_y and α_J presented in Tables 2 ($C_s = 0.159$), 3 ($C_s = 0.0636$) and 4 ($C_s = 0.0318$), respectively. As seen, the coil efficiency η for $C_s = 0.0318$ has better gradient uniformity than those for both $C_s = 0.159$ and $C_s = 0.0636$.

Figure 7 shows the coil layouts obtained for different values of the current density regularization weight, α_J, and the intra-slice gradient uniformity parameter, C_s, with the anterior–posterior gradient variation parameter fixed at $C_y = 0.16$, providing insight into the fabrication complexity of the resulting designs. In all cases, the stream-function distributions exhibit a similar global topology, characterized by dominant positive and negative regions separated by a smooth

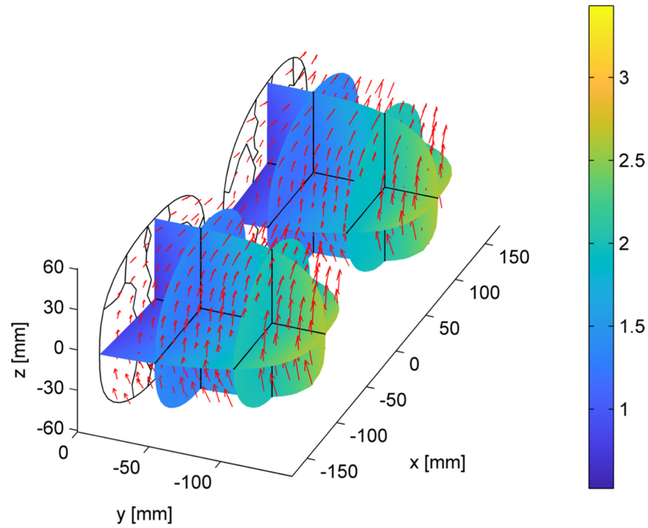

(a) α_J = 5.49e-3 and C_y = 0.119

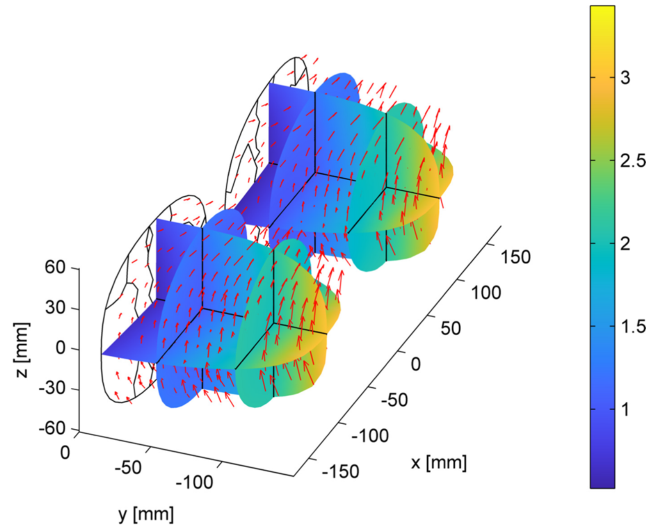

(b) α_J = 1.26e-3 and C_y = 0.16

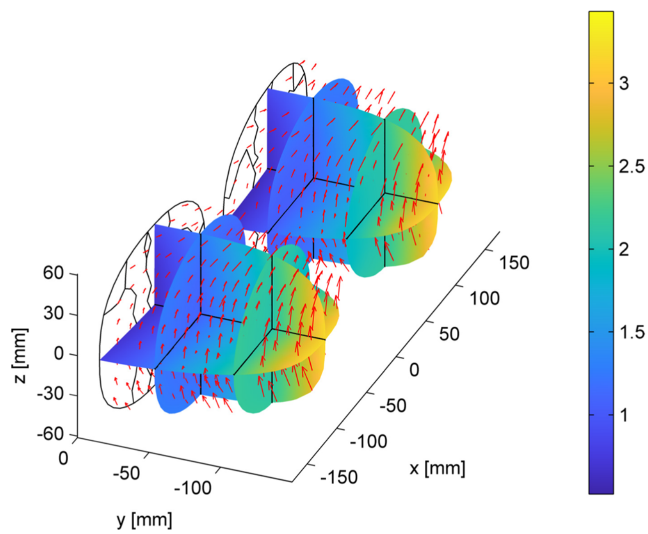

(c) α_J = 7.13e-3 and C_y = 0.16

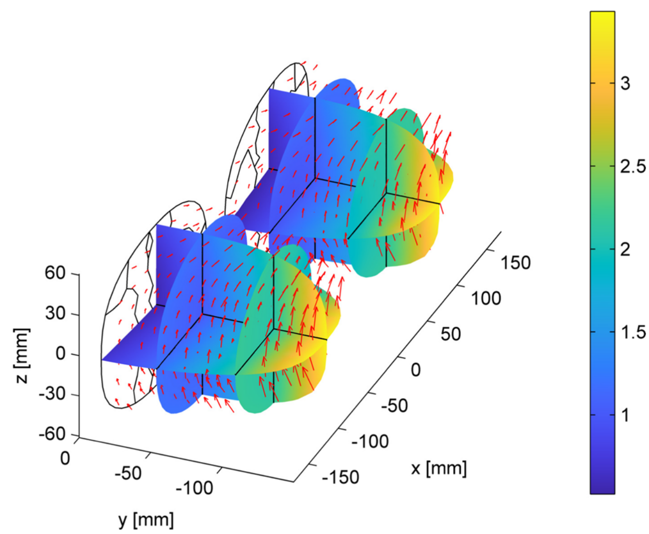

(d) α_J = 4.44e-3 and C_y = 0.182

Fig. 6 Spatial distributions of coil efficiency η [mT/m/A] (color map) for different values of the current density regularization weight, α_J, and the anterior–posterior gradient variation parameter, C_y, with the intra-slice gradient uniformity parameter fixed at $C_s = 0.0318$. The gradient vectors of the magnetic field B_z per unit current are indicated by red arrows

transition zone. The corresponding isolines form continuous and well-organized winding paths over the coil surface, indicating that all designs generate magnetic fields with similar spatial encoding characteristics, as illustrated in Figs. 4d, 5c, 6c, d.

Despite these similarities, a notable difference among the designs is the increase in the dynamic range of the stream function, $(\psi_{\max} - \psi_{\min})$, as C_s decreases. This trend indicates that a larger current circulation is required to satisfy the increasingly stringent coronal-slice constraint. Consequently, for a fixed number of contours, the operating current increases from 25.4 A for the design with $C_s = 0.159$ to 31.0 A and 36.1 A for the designs with $C_s = 0.0636$ and $C_s = 0.0318$, respectively. For the design with $C_s = 0.0318$ and a larger current-density weighting factor, $\alpha_J = 7.13 \times 10^{-3}$, the operating current decreases slightly to 34.7 A owing to the regularization effect of the current-density penalty term.

Prototype and field map measurement

To reduce the difficulty of in-house coil fabrication, the coil designed with $C_s = 0.0318$, $C_y = 0.16$ and $\alpha = 1.26e-3$ was realized experimentally. Figure 8 depicts the simulated magnetic field B_z^s and measured magnetic field B_z^m generated

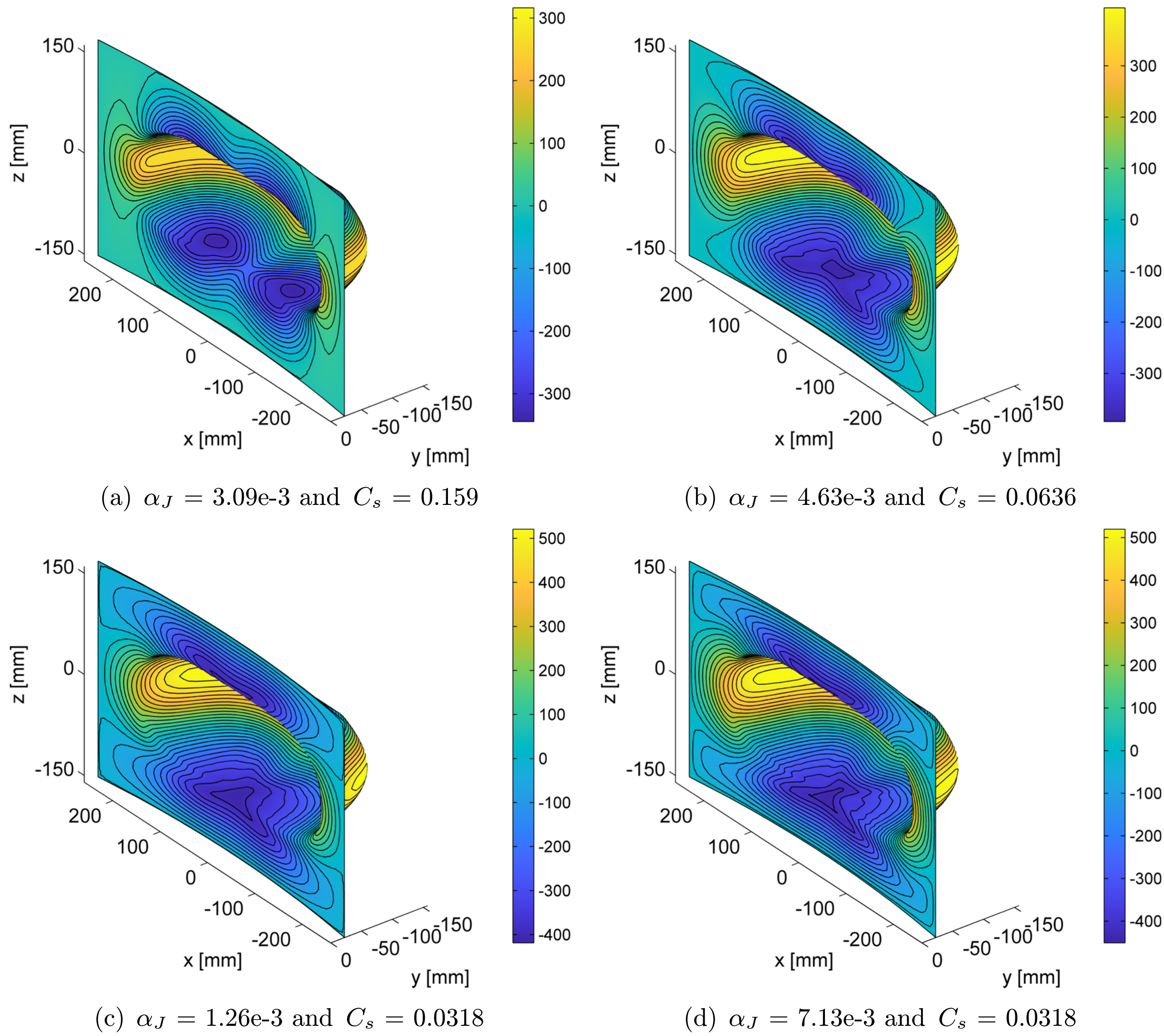

Fig. 7 Spatial distributions of the resulting stream function ψ (unit: amperes [A]) for different values of the current density regularization weight, α_J, and the intra-slice gradient uniformity parameter, C_s, with the anterior–posterior gradient variation parameter fixed at $C_y = 0.16$. The continuous black contour lines (isolines) define the optimized coil winding layouts

by the built coil, respectively. As can be seen, the measured results match with the simulated fields well. The relative errors of the magnetic field (Fig. 8c) are less than 7.98% over the whole phantom. These deviations may arise from manufacturing imperfections.

The contour distribution of B_z^s (Fig. 8d) on the characteristic plane reveals a nearly uniform magnetic-field gradient across the coronal slice of the ROI, indicating good local encoding-field characteristics. Moreover, the isoline representation enables a clearer visualization of regions where the field begins to deviate from the desired behavior near the coil boundaries, thereby illustrating the practical limits of the coil performance.

The measured coil resistance was 271 mΩ, which is substantially larger than the simulated value of 30.3 mΩ, primarily because the fabricated coil employed Litz wire (0.2 mm × 105 strands) rather than the 3 mm-thick copper plate assumed in the design. The measured coil inductance of 129 μH agrees well with the simulated value, with a relative error of around 7%. In general, the results demonstrate the validity of our design method.

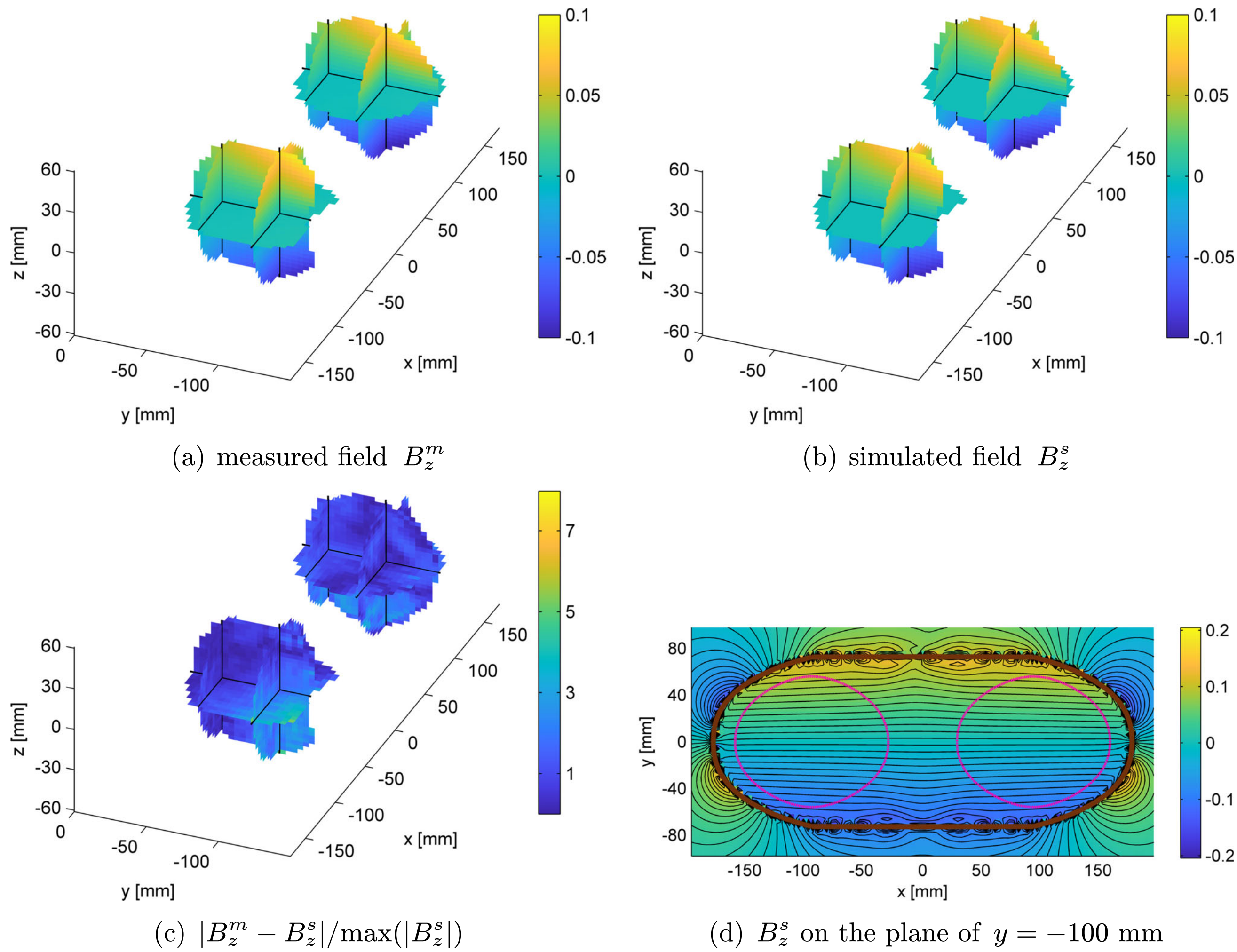

Fig. 8 Comparison of the measured (**a**) and simulated (**b**) B_z fields (unit: [mT]) at an applied coil current of 1 A. The measured field B_z^m is obtained from the fabricated prototype and the simulated field B_z^s is calculated using the coil layout shown in Fig. 7b. The relative errors (%) between the two fields are shown in **c**. The isoline map of B_z^s (unit: [mT]) on the characteristic plane at $y = -100$ mm is shown in **d**, illustrating the magnetic field quality. The coil boundary is indicated by dark copper-colored lines, while the boundaries of the ROI are denoted by magenta lines

Discussion

This study presents a novel optimization strategy for controlling the variation of gradient magnitude along the y-axis in nonlinear breast gradient coils. The introduction of a wire-width-based figure of merit allows the performance of nonlinear coil designs to be evaluated in a way that accounts for both coil efficiency and engineering constraints, such as minimum wire width. In addition, the coefficient of variation of coil efficiency η is employed as a metric to assess the spatial uniformity of gradient strength inside coronal slices or over the ROI. The effectiveness of the proposed framework was demonstrated through a series of numerical examples and validated with experimental results, highlighting its potential for designing high-performance, localized gradient systems for diffusion-weighted breast imaging.

The use of the coefficient of variation of the coil efficiency as a performance indicator provides a direct and spatially resolved measure of uniformity. Notably, as shown in Fig. 3, the designs optimized with $C_s = 0.0318$ achieve intra-slice uniformity levels that are comparable to, or even better than, those of the conventional linear G_z coil ($\mathrm{CV}_{\mathrm{ROI}} = 0.102$, Table 1), while still offering the spatial selectivity advantages of nonlinear encoding. These results underscore the utility of the proposed formulation for balancing efficiency, manufacturability, and spatial uniformity in the design of next-generation nonlinear breast gradient coils.

Although increasing C_y generally increases gradient variation along the y-axis, Fig. 3 indicates that its influence on CV_s is not uniform across all coronal slices. This observation may be attributed to the definition of the per-slice constraint (4), which is defined over the entire ROI rather than on a slice-by-slice basis. To better control the spatial uniformity of gradient variation within individual slices, an improved formulation could incorporate additional constraints on selected representative coronal slices. This direction will be explored in future work.

Figure 7b illustrates the coil layout of the constructed prototype. Notably, a significant number of windings are positioned along the rim, close to the chest region. As a result, the coil may generate elevated electric fields in thoracic tissues, potentially leading to peripheral nerve stimulation or cardiac stimulation. To evaluate the safety of the prototype for in vivo use, the effects of PNS and the induced electric field in the heart region will be simulated using the method described in [27] in the near future. Moreover, experimental PNS assessments will also be conducted to evaluate subject safety in future work.

The present designs utilize an unshielded topology for two primary reasons. First, unshielded configurations maximize the achievable gradient strength for a defined minimum wire width, generally offering more coil efficiency compared to shielded variants. Second, as the local coil is positioned relatively far away from the cryostat, only minor eddy-current induction is expected. If eddy-current effects prove non-negligible in diffusion-weighted imaging, two mitigation strategies remain available for future exploration. These include redesigning the system with active shielding or implementing compensation techniques via linear gradient coils, as detailed in [28].

An initial prototype based on the proposed approach has been fabricated in-house [24]. Figure 8 shows agreement between simulated and measured magnetic fields, confirming the validity of the design process. As this report focuses on the theoretical framework, other characterizations of the prototype's physical properties including thermal performance, eddy current behavior, PNS thresholds, acoustics and imaging – are currently in progress and will be detailed in a subsequent publication.

Conclusion

This study introduced and validated a new optimization method for designing non-linear breast gradient coils for diffusion-weighted MRI in breast cancer screening. By adding a y-axis constraint and a wire-width-based figure of merit we were able to improve coil efficiency and spatial uniformity near the posterior breast region which is the most challenging area to image. Experimental results show the feasibility and accuracy of these designs and their potential for clinical use. Future work will look into safety and refine the coil performance, especially manufacturing and physiological limitations.

Acknowledgements This work was supported by the German Research Foundation (DFG) Project number 468440804 "High-Power Diffusion Probe for Human Breast MRI – Phase 2" and the Eurostars 3 Project number 3325 "FEM-SCAN: Fast and Efficient MRI Scanning for breast cancer detection".

Funding Open Access funding enabled and organized by Projekt DEAL. This study was funded by the German Research Foundation (DFG) Project number 468440804 "High-Power Diffusion Probe for Human Breast MRI – Phase 2" and the Eurostars 3 Project number 3325 "FEM-SCAN: Fast and Efficient MRI Scanning for breast cancer detection".

Availability of data and materials The data that support the findings of this study are not openly available due to intellectual property restrictions, but are available from the corresponding author upon reasonable request. Data are located in controlled access data storage at University Medical Center Freiburg.

Declarations

Conflict of interest All authors declare that they have no conflict of interest.

Ethical approval All procedures performed in studies involving human participants were in accordance with the ethical standards of the institutional and/or national research committee and with the 1964 Helsinki declaration and its later amendments or comparable ethical standards.

Informed consent Informed consent was obtained from all individual participants included in the study.

References

1. Iima M, Le Bihan D (2023) The road to breast cancer screening with diffusion MRI. Front Oncol 13:993540. https://doi.org/10.3389/fonc.2023.993540
2. Partridge SC, Nissan N, Rahbar H, Kitsch AE, Sigmund EE (2017) Diffusion-weighted breast MRI: clinical applications and emerging techniques. J Magn Reson Imaging 45(2):337–355. https://doi.org/10.1002/jmri.25479
3. Baxter GC, Graves MJ, Gilbert FJ, Patterson AJ (2019) A meta-analysis of the diagnostic performance of diffusion MRI for breast lesion characterization. Radiology 291(3):632–641. https://doi.org/10.1148/radiol.2019182510

4. Molendowska M, Palombo M, Foley KG, Narahari K, Fasano F, Jones DK, Alexander DC, Panagiotaki E, Tax CMW (2024) Diffusion MRI in prostate cancer with ultra-strong whole-body gradients. NMR Biomed 37(12):e5229. https://doi.org/10.1002/nbm.5229
5. Baltzer P, Mann RM, Iima M, Sigmund EE, Clauser P, Gilbert FJ, Martincich L, Partridge SC, Patterson A, Pinker K, Thibault F, Camps-Herrero J, Le Bihan D, On behalf of the EUSOBI international Breast Diffusion-Weighted Imaging Working Group (2020) Diffusion-weighted imaging of the breast—a consensus and mission statement from the EUSOBI International Breast Diffusion-Weighted Imaging Working Group. Eur Radiol 30(3):1436–1450. https://doi.org/10.1007/s00330-019-06510-3
6. Laun FB, Kuder TA, Wetscherek A, Stieltjes B, Semmler W (2012) NMR-based diffusion pore imaging. Phys Rev E 86(2):021906. https://doi.org/10.1103/PhysRevE.86.021906
7. Setsompop K, Kimmlingen R, Eberlein E, Witzel T, Cohen-Adad J, McNab JA, Keil B, Tisdall MD, Hoecht P, Dietz P, Cauley SF, Tountcheva V, Matschl V, Lenz VH, Heberlein K, Potthast A, Thein H, Van Horn J, Toga A, Schmitt F, Lehne D, Rosen BR, Wedeen V, Wald LL (2013) Pushing the limits of in vivo diffusion MRI for the human connectome project. Neuroimage 80:220–233. https://doi.org/10.1016/j.neuroimage.2013.05.078
8. Lasič S, Oredsson S, Partridge SC, Saal LH, Topgaard D, Nilsson M, Bryskhe K (2016) Apparent exchange rate for breast cancer characterization. NMR Biomed 29(5):631–639. https://doi.org/10.1002/nbm.3504
9. Jones DK, Alexander DC, Bowtell R, Cercignani M, Dell'Acqua F, McHugh DJ, Miller KL, Palombo M, Parker GJM, Rudrapatna US, Tax CMW (2018) Microstructural imaging of the human brain with a 'super-scanner': 10 key advantages of ultra-strong gradients for diffusion MRI. Neuroimage 182:8–38. https://doi.org/10.1016/j.neuroimage.2018.05.047
10. Ludwig D, Laun FB, Klika KD, Rauch J, Ladd ME, Bachert P, Kuder TA (2022) Diffusion pore imaging in the presence of extraporal water. J Magn Reson 339:107219. https://doi.org/10.1016/j.jmr.2022.107219
11. Zhang B, Yen Y-F, Chronik BA, McKinnon GC, Schaefer DJ, Rutt BK (2003) Peripheral nerve stimulation properties of head and body gradient coils of various sizes. Magn Reson Med 50(1):50–58. https://doi.org/10.1002/mrm.10508
12. Tan ET, Hua Y, Fiveland EW, Vermilyea ME, Piel JE, Park KJ, Ho VB, Foo TKF (2020) Peripheral nerve stimulation limits of a high amplitude and slew rate magnetic field gradient coil for neuroimaging. Magn Reson Med 83(1):352–366. https://doi.org/10.1002/mrm.27909
13. Jia F, Littin S, Amrein P, Yu H, Magill AW, Kuder TA, Bickelhaupt S, Laun F, Ladd ME, Zaitsev M (2021) Design of a high-performance non-linear gradient coil for diffusion weighted MRI of the breast. J Magn Reson 331:107052. https://doi.org/10.1016/j.jmr.2021.107052
14. Littin S, Jia F, Amrein P, Yu H, Magill AW, Kuder TA, Ladd ME, Laun F, Bickelhaupt S, Zaitsev M (2020) Single channel non-linear breast gradient coil for diffusion encoding. In: Proceedings of the 2020 ISMRM virtual conference and exhibition, p 1134
15. Poole MS, While PT, Lopez HS, Ng M, Crozier S (2010) Minimax current density coil design. J Phys D Appl Phys 43(9):095001. https://doi.org/10.1088/0022-3727/43/9/095001
16. Turner R (1988) Minimum inductance coils. J Phys E: Sci Instrum 21(10):948–952. https://doi.org/10.1088/0022-3735/21/10/008
17. Sanchez H, Liu F, Trakic A, Crozier S (2007) A simple relationship for high efficiency-gradient uniformity tradeoff in multilayer asymmetric gradient coils for magnetic resonance imaging. IEEE Trans Magn 43(2):523–532. https://doi.org/10.1109/TMAG.2006.887177
18. Jia F, Littin S, Layton KJ, Kroboth S, Yu H, Zaitsev M (2017) Design of a shielded coil element of a matrix gradient coil. J Magn Reson 281:217–228. https://doi.org/10.1016/j.jmr.2017.06.006
19. Jia F, Liu Z, Korvink JG (2011) A novel coil design method for manufacturable configurations at optimal performance. In: Proceedings of the ISMRM 20th scientific meeting and exhibition, Montreal, p 3780
20. Littin S, Kuder TA, Jia F, Magill AW, Amrein P, Laun F, Bickelhaupt S, Klein V, Ladd ME, Zaitsev M (2021) Approaching order of magnitude increase of gradient strength: non-linear breast gradient coil for diffusion encoding. In: Proceedings of the 2021 ISMRM virtual conference and exhibition, p 3096
21. Peeren GN (2003) Stream function approach for determining optimal surface currents. J Comput Phys 191(1):305–321. https://doi.org/10.1016/S0021-9991(03)00320-6
22. Lemdiasov RA, Ludwig R (2005) A stream function method for gradient coil design. Concepts Magn Reson Part B Magn Reson Eng 26B(1):67–80. https://doi.org/10.1002/cmr.b.20040
23. Amrein P, Jia F, Zaitsev M, Littin S (2022) CoilGen: Open-source MR coil layout generator. Magn Reson Med 88:1465–1479. https://doi.org/10.1002/mrm.29294
24. Arends GC, Versteeg E, Jia F, Valentijn R, Cooijmans ED, Klomp DJ, Zaitsev M, Tax CM, Littin S (2025) Bilateral breast gradient insert prototype for strong diffusion encoding at 3T. In: Proceedings of 2025 ISMRM-ISMRT annual meeting and exhibition, Honolulu, Hawaii, p 1339
25. Arends GC, Versteeg E, Jia F, Klomp DJ, Zaitsev M, Littin S, Tax CM (2026) Towards high-performance breast diffusion MRI: evaluation of temperature, nerve stimulation, and diffusion measurements. In: Proceedings of 2026 ISMRM-ISMRT annual meeting and exhibition, Cape Town, p 1766
26. Welz AM, Cocosco C, Dewdney A, Gallichan D, Jia F, Lehr H, Liu Z, Post H, Schmidt H, Schultz G, Testud F, Weber H, Witschey W, Korvink J, Hennig J, Zaitsev M (2013) Development and characterisation of an unshielded PatLoc gradient coil for human head imaging. Concepts Magn Reson Part B Magn Reson Eng 43B:111–125. https://doi.org/10.1002/cmr.b.21244
27. Jia F, Endt AV, Amrein P, Russe MF, Rohdjess H, Leghissa M, Zaitsev M, Littin S (2025) Initial assessment of PNS safety for interventionalists during image-guided procedures. Magn Reson Mater Phy 38:239–251. https://doi.org/10.1007/s10334-025-01228-4
28. van der Velden TA (2017) Novel techniques for 7 Tesla breast MRI. http://dspace.library.uu.nl/handle/1874/351284